Available online at www.sciencedirect.com
SCIENCE DIRECT®
Journal of Computational Physics 204 (2005) 1–26
JOURNAL OF COMPUTATIONAL PHYSICS
www.elsevier.com/locate/jcp

Heterogeneous multiscale method for the modeling of complex fluids and micro-fluidics

Weiqing Ren *, Weinan E

Department of Mathematics and PACM, Princeton University, Fine Hall, Princeton, NJ 08544, USA

Received 8 January 2004; received in revised form 2 July 2004; accepted 4 October 2004
Available online 2 November 2004

Abstract

The framework of the heterogeneous multiscale method (HMM) is used to develop numerical methods for the study of macroscale dynamics of fluids in situations, where either the constitutive relation or the boundary conditions are not explicitly available and have to be inferred from microscopic models such as molecular dynamics. Continuum hydrodynamics is used as the macroscopic model, while molecular dynamics serves as the microscopic model and is used to supply the necessary data, e.g., the stress or the boundary condition, for the macroscopic model. Scale separation is exploited so that the macroscopic variables can be evolved in macroscopic spatial/temporal scales using data that are estimated from molecular dynamics simulation on microscale spatial/temporal domains. This naturally decouples the micro and macrospatial and temporal scales whenever possible. Applications are presented for models of complex fluids, contact line dynamics, and a simple model of non-trivial fluid–solid interactions.

1. Introduction

Continuum hydrodynamics has had rather impressive success in modeling the behavior of fluids, from turbulent flows, to high Mach number gas dynamics, to the spreading of liquid films. It is remarkable that very simple constitutive relations and boundary conditions, with all molecular details left out except for very few parameters such as viscosity, perform so well in such a wide variety of situations. Nevertheless, there are still many problems for which such continuum models are not adequate. In most cases, the difficulty arises either from the complex nature of the constituting molecules such as in polymeric fluids, or from the geometric size of the problem as in micro- or nano-fluidics, or from the complex interactions or chemical reactions

* Corresponding author.
E-mail addresses: weiqing@math.princeton.edu (W. Ren), weinan@math.princeton.edu (W. E).

0021-9991/$ - see front matter
doi:10.1016/j.jcp.2004.10.001

at the fluid–fluid or fluid–solid interface. In these situations, it is natural to describe the process using a more detailed model such as molecular dynamics (MD). However too often it is impossible to perform full MD simulations under realistic physical conditions, due to the disparate spatial and temporal scales that have to be resolved in such simulations. It is therefore desirable to develop hybrid numerical methods that are based on a combination of the continuum and molecular formulations, in order to take the advantage of both the efficiency of the continuum models and the accuracy of the molecular models. Indeed this has been the theme of much recent work [2–7] and is again the theme of the present paper.

Our starting point is the framework of the heterogeneous multiscale method (HMM) [1] which provides a general and convenient setup for developing hybrid atomistic-continuum methods. HMM starts with an unclosed macroscopic model which for the present problem will simply be the conservation laws of mass and momentum. There are two main components in HMM: choosing a macro solver for the macroscale variables and estimating the needed data from the micro model. The macro solver should be carefully chosen to facilitate the coupling with the micro model. The general procedure of solving dynamical problems using HMM is as follows. Assume that we have the macro variable $U(t)$, for example, the velocity field, at time t. To calculate the macro variable at the next time step $t + \Delta t$, we estimate the data needed in the macro solver, for example the momentum flux, from the micro model such as molecular dynamics. In order for the micro state to be consistent with the local macro state, certain constraints are imposed in the micro model, usually through the imposition of some boundary conditions. The microscopic data are then processed using ensemble, spatial and temporal averaging to provide the needed macroscale data. These data are finally passed back to the macro solver and $U(t + \Delta t)$ is calculated.

In this paper, we apply the framework of HMM to develop numerical methods for the study of two types of problems in fluids: The first type, which are type-A problems as defined in [1], are problems for which the boundary condition needs to be extracted from microscopic models. Examples include contact line dynamics, problems with complex fluid–solid interactions and surface reactions. The second type, called type-B problems, are problems for which the constitutive relations have to be extracted from microscopic models. Polymeric fluids serve as examples of this type. For type-A problems, the boundary conditions are obtained from local MD simulation at the boundary. For type-B problems, the stresses are calculated from MD simulations at locations where they are needed in the macro solver, e.g., at cell boundaries if the continuum equations are solved using finite volume methods.

Several hybrid methods have been developed in recent years, mainly for type-A problems. Hadjiconstantinou and Patera used the flow field measured in MD simulations as the boundary condition for continuum computations [3,4]. The particle velocities are constrained through momentum reservoirs based on the continuum velocity field. The Schwartz iteration method is used to ensure that the two descriptions are consistent in an overlapping region at the steady state. They used this approach to study a steady channel flow with an obstacle and the contact line dynamics. The coupled continuum/MD method developed by Li and co-workers [7] is also based on the alternating Schwartz method, but pays more attention to the microscopic physics. They developed an algorithm called the thermodynamic field estimator to infer the continuum boundary condition from MD calculation. A particle velocity transformation called the optimal particle controller is imposed on the boundary of the MD sub-domain in order to achieve the desired field in MD calculation. O'Connell and Thompson simulated Couette flow by coupling a MD simulation to a continuum computation. The coupling is achieved by constraining the dynamics of fluid particles in the vicinity of the MD-continuum interface [2]. Flekkoy, Wagner and Feder introduced a hybrid method that aimed at keeping the fluxes of the conserved quantities continuous across the MD-continuum interface [5]. An improved version is introduced recently by Nie and co-workers, in which the matching conditions in the overlapping region were imposed using Lagrange multipliers [6]. In such a coupling scheme, the time scales of the molecular and continuum simulations are still coupled, and this is a major limitation.

All these methods are based on the idea of domain decomposition (see Fig. 1(a)). The continuum model is solved in one part of the domain while molecular dynamics is solved in another part, usually around the

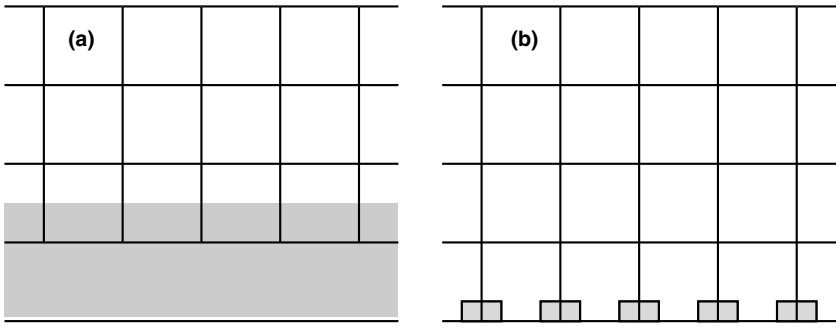

Fig. 1. (a) Schematic of the domain decomposition type of methods for type-A problems. The Navier–Stokes equations are solved in the region covered with grid, and MD is carried out in the shaded region. These two regions are joined by an overlapping region in which field variables or fluxes are matched . (b) Schematic of the method developed in this paper. The whole domain is covered by the macrosolver, and the boundary conditions are built by constrained MD simulation in the shaded region at the boundary.

boundary. An overlapping region is used between these two domains in which the two descriptions are forced to match each other by either constrained molecular dynamics or Schwartz iteration. At the present time, these methods have had limited success for dynamic problems due to the coupling of the time scales and the complexity of the algorithms.

The method developed here is different from the overlapping domain decomposition strategy in that the whole computational domain is covered by a macroscopic grid on which a macro solver is imposed (see Fig. 1(b)). The microscale model enters as a local refinement for obtaining the data needed in the macro solver. By choosing appropriate macro-scale solvers, the task of coupling with the micro-scale model is considerably simplified. The macro and micro time steps are naturally decoupled in our method, and large scale dynamical problems can be studied as we demonstrate later. Additional discussions on the time-scale issue are presented in the conclusion part of this paper.

This paper is organized as following. We discuss the macro and micro models in Section 2. Numerical methods and examples for type-B problems are presented in Section 3. In Section 4 we describe the numerical methods for type-A problems with applications to contact line dynamics, as well as a Marangoni flow. Some concluding remarks are made in Section 5.

2. Macroscopic and microscopic models

At the continuum level, the dynamics of incompressible flow have to obey conservation of mass and momentum:

$$\begin{cases} \rho \mathbf{u}_t + \nabla \cdot \tau = 0, \\ \nabla \cdot \mathbf{u} = 0, \end{cases} \tag{1}$$

where the momentum flux $\tau = \rho \mathbf{u} \otimes \mathbf{u} + p\, I - \tau_d$. Here ρ is the density of the fluid, $\mathbf{u} = (u, v)$ is the velocity field, and p is the pressure, τ_d is the viscous stress tensor. At this level, the system is not closed since the stress tensor is yet to be specified. For fluids with simple molecular structures, the simple constitutive relation

$$\tau_d = \mu(\nabla \mathbf{u} + \nabla \mathbf{u}^{\mathrm{T}}) \tag{2}$$

is accurate enough for almost all purposes. However if the molecular structure becomes more complex, such as the case of polymeric fluids, (2) is no longer accurate. As we show later, in this case, one can still calculate the stress from atomistic models, for example using the Irving–Kirkwood formula.

Another important component in the model is the boundary condition. Almost all macroscopic models assume the no-slip boundary condition

$$\mathbf{u} = \mathbf{u}_0, \tag{3}$$

where $\mathbf{u}_0$ is the velocity of the boundary. At the microscopic level, the dynamics of the fluid is described by the position and momentum of all constituting particles, which are governed by Newton's law:

$$\begin{cases} m_i \dot{\mathbf{q}}_i(t) = \mathbf{p}_i(t), \\ \dot{\mathbf{p}}_i(t) = \mathbf{F}_i, \end{cases} \tag{4}$$

$i = 1, 2, \ldots, N$. Here m_i is the mass of the ith particle, $\mathbf{q}_i$ and $\mathbf{p}_i$ are its position and momentum respectively, $\mathbf{F}_i$ is the force acting on the ith particle.

To examine the behavior of the fluid flow near a solid boundary, we should also model the vibration of the atoms in the solid next to the fluid–solid interface. Therefore one should consider the fluid–solid system as a whole.

To integrate the set of equations in (4), we use the velocity-Verlet algorithm. Computational cost can be reduced by using the linked-cell list or the Verlet list for short-ranged interactions [8,9].

In the simulation of viscous flow, the temperature of the system can change significantly, due to the heat generated by viscous dissipation or friction between the fluids and the solids at the boundary. One way of controlling temperature is to rescale the thermal velocity of each particle at regular time intervals. This method is easy to implement but is rather unphysical. An alternative approach is to use the Nosé-Hoover thermostat in which the system is coupled with an artificial heat bath, represented by an additional degree of freedom [8,9]. We use this latter approach.

Given a microscopic state of the system $\{\mathbf{q}_i(t), \mathbf{p}_i(t)\}_{i=1,2,\ldots,N}$, we define the empirical momentum distribution

$$\mathbf{m}(\mathbf{x}, t) = \sum_i \mathbf{p}_i(t) \delta(\mathbf{q}_i(t) - \mathbf{x}), \tag{5}$$

where δ is the Delta function. Momentum conservation can then be expressed in terms of the microscopic variables as:

$$\mathbf{m}_t + \nabla \cdot \tau(\mathbf{x}, t) = 0, \tag{6}$$

where the momentum current density $\tau(\mathbf{x}, t)$ is given by the following Irving–Kirkwood expression [11]:

$$\tau(\mathbf{x}, t) = \sum_i \frac{1}{m_i} (\mathbf{p}_i \otimes \mathbf{p}_i) \delta(\mathbf{q}_i - \mathbf{x}) + \frac{1}{2} \sum_{j \neq i} \left((\mathbf{q}_i - \mathbf{q}_j) \otimes \mathbf{F}_{ij} \right) \int_0^1 \delta(\lambda \mathbf{q}_i + (1-\lambda)\mathbf{q}_j - \mathbf{x}) \, \mathrm{d}\lambda, \tag{7}$$

where $\mathbf{F}_{ij}$ is the force acting on the ith particle by the jth particle.

An important issue in molecular dynamics is how to model the atomistic forces. This can be a rather difficult problem. Fortunately the algorithms we develop in this paper are quite insensitive to the details of the atomistic potential. Therefore to avoid unnecessary complications we will restrict ourselves to the simplest model, namely the Lennard-Jones (LJ) potential in a slightly modified form:

$$V^{\mathrm{LJ}}(r) = 4\varepsilon \left(\left(\frac{\sigma}{r} \right)^{12} - \eta \left(\frac{\sigma}{r} \right)^{6} \right). \tag{8}$$

Here r is the distance between particles, ε and σ are characteristic energy and length scales. The parameter η controls the nature of the interaction between particles. When $\eta = 1$, (8) defines the usual LJ potential which is attractive at long distance. Repulsion between particles of different species can be modeled using negative values of η.

Assuming pairwise interaction such as in (8), the interparticle force is given by

$$\mathbf{F}_i = -\sum_{i \neq j} \nabla V^{\mathrm{LJ}}(|\mathbf{q}_i(t) - \mathbf{q}_j(t)|). \tag{9}$$

To reduce the cost for computing the sum, the tail of the potential is cut off at a distance $r_c = 2.5\sigma$.

For a physical discussion on the origin of the molecular forces, we refer to [21].

We will express all quantities in the numerical examples in reduced atomic units. The unit of length is σ. The unit of time is $\sigma\sqrt{m/\varepsilon}$. For temperature it is ε/k_B where k_B is the Boltzmann constant, and for density it is m/σ^2 in 2d fluids and m/σ^3 in 3D fluids. The unit of viscosity is $(\varepsilon m)^{1/2}/\sigma$ in 2d and $(\varepsilon m)^{1/2}/\sigma^2$ in 3D. The unit of surface tension is ε/σ^2. For simplicity we will restrict ourselves to macroscopically two-dimensional systems. But most of our molecular dynamics calculations are done in three dimensions.

3. Type-B problems: atomistic-based constitutive modeling

3.1. Macroscopic solver

As the macroscopic solver for the conservation laws, we choose the projection method on a staggered grid [20]. The projection method is a fractional step method. At each time step, we first discretize the time derivative in the momentum equation by the forward Euler scheme:

$$\rho \frac{\tilde{\mathbf{u}}^{n+1} - \mathbf{u}^n}{\Delta t} + \nabla \cdot \tau^n = 0, \tag{10}$$

where τ^n is the momentum flux. For the moment, pressure as well as the incompressibility condition are neglected. Next the velocity field $\tilde{\mathbf{u}}^n + 1$ is projected onto the divergence-free subspace:

$$\rho \frac{\mathbf{u}^{n+1} - \tilde{\mathbf{u}}^{n+1}}{\Delta t} + \nabla p^{n+1} = 0, \tag{11}$$

where p^{n+1} is determined by

$$\Delta p^{n+1} = \frac{\rho}{\Delta t} \nabla \cdot \tilde{\mathbf{u}}^{n+1} \tag{12}$$

usually with Neumann boundary condition.

The spatial discretization is shown in Fig. 2. For integer values of i and j, we define u at $(x_i, y_{j+\frac{1}{2}})$, v at $(x_{i+\frac{1}{2}}, y_j)$, and p at the cell center $(x_{i+\frac{1}{2}}, y_{j+\frac{1}{2}})$. The diagonals of the flux τ are defined at $(x_{i+\frac{1}{2}}, y_{j+\frac{1}{2}})$, and the off-diagonals are defined at (x_i, y_j). The operators $\nabla$and Δ are discretized by standard central difference and five-point formula respectively. The use of this grid simplifies the coupling with molecular dynamics.

3.2. Estimating the stress

The data that we need in the macroscopic solver and should be estimated from molecular dynamics are the stresses. In this subsection, we discuss how this is done.

3.2.1. Constrained microscopic solver: constant rate-of-strain MD

At each point where the macroscopic stress is needed, a local molecular dynamics calculation will be carried out to provide the stress. Constraints have to be imposed on the molecular dynamics calculation in order to ensure that the results are consistent with the local macroscopic state. These constraints are usually imposed in the form of Lagrange multipliers or boundary conditions.

Our aim is to calculate the viscous stress by taking spatial and temporal averages over a large number of time steps after the atomistic system is relaxed. However, maintaining the system under stress in a statistical

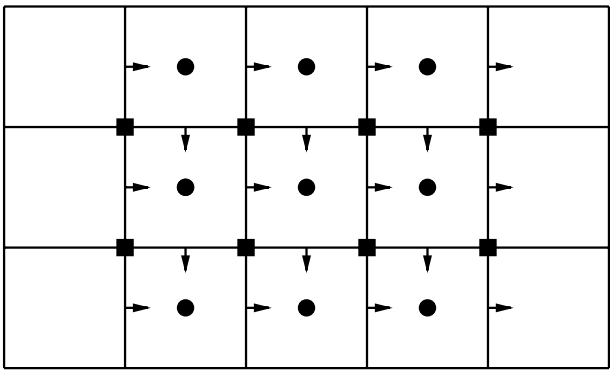

Fig. 2. Schematic of the spatial discretization of the continuum equations in (1). u is defined at $(x_i, y_{j+\frac{1}{2}})$, v is defined at $(x_i+\frac{1}{2}, y_j)$, and p is at the cell center $(x_i+\frac{1}{2}, y_j+\frac{1}{2})$. τ_{11} and τ_{22} are calculated at the cell center indicated by circles, and τ_{12} is calculated at the grid points indicated by squares.

steady state, from which the non-equilibrium averages of certain quantities are computed, represents a significant challenge. Since the viscous stress is expected to depend on the velocity gradient, we need to set up and maintain a steady linear velocity profile, with a specified gradient from the continuum calculation. This constrained dynamics is achieved through imposing appropriate boundary conditions on the simulation box. To minimize the finite size effect, periodic boundary condition is commonly used in the study of equilibrium properties. However, in the current situation where there is momentum transport, the conventional periodic boundary conditions need to be modified.

There exists an earlier work due to Lees and Edwards [10] in which the periodic boundary condition is modified to maintain a constant shear in one direction. This is done by shifting the periodic copies above and below the simulation box in opposite directions according to the given shear profile. Here we extend this idea to situations with a general linear velocity profile.

Without loss of generality, we will consider the situation when the macroscopic velocity profile is of the form

$$\begin{pmatrix} u \\ v \\ w \end{pmatrix} = \begin{pmatrix} a & b & 0 \\ c & -a & 0 \\ 0 & 0 & 0 \end{pmatrix} \begin{pmatrix} x \\ y \\ z \end{pmatrix} = A\mathbf{x}. \tag{13}$$

To initialize the MD calculation, one may simply start with a perfect lattice configuration in a rectangular box. Each particle is given a velocity according to (13), plus a random component with mean 0 and variance $k_B\,T$, where T is the desired temperature and k_B is the Boltzmann constant.

Deforming the simulation box. Periodic boundary condition is imposed on a dynamically deforming simulation box, whose vertices move according to

$$\dot{\mathbf{x}} = A\mathbf{x}, \quad A = \begin{pmatrix} a & b & 0 \\ c & -a & 0 \\ 0 & 0 & 0 \end{pmatrix}. \tag{14}$$

In the z-direction there is no velocity gradient, hence the conventional periodic boundary condition is used. (Recall that the macroscopic velocity profile is 2D, but the MD is 3D). Intuitively it is helpful to think of the simulation box as been embedded in the whole space.

The shape of the deformed box at a latter time is shown in Fig. 3(b). Suppose at this point a particle crosses the boundary at $P(\mathbf{x})$, with velocity $\mathbf{u}$, it will return to the box at $P'(\mathbf{x}')$ with modified velocity

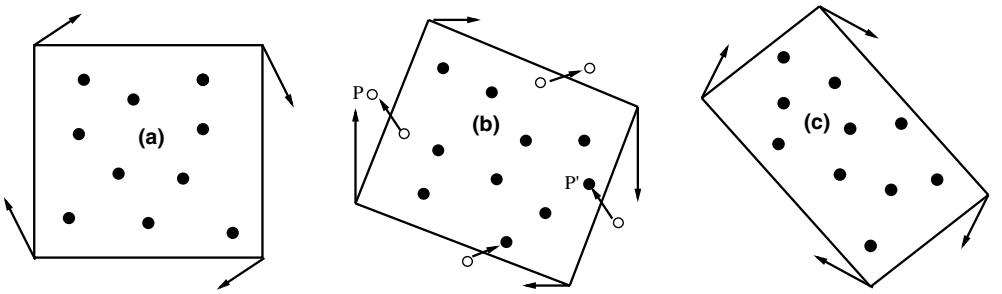

Fig. 3. Periodic boundary conditions on a dynamically deforming box.

$$\mathbf{u}' = \mathbf{u} + A(\mathbf{x}' - \mathbf{x}), \tag{15}$$

where P' is the periodic image of P with respect to the deformed box. It should be emphasized that the set-up and maintenance of the given velocity gradient are achieved by allowing the simulation box to change shape as well as the modification of the periodic boundary conditions.

It is easy to see that if the velocity field is a pure shear

$$A = \begin{pmatrix} 0 & b & 0 \\ 0 & 0 & 0 \\ 0 & 0 & 0 \end{pmatrix} \tag{16}$$

then this boundary condition becomes simply the Lees-Edwards boundary condition.

Reinitialization. As the simulation proceeds, the simulation box will in general become quite elongated in one direction and narrowed in the other direction (see Fig. 3(c)). If the box is significantly deformed, we need to reinitialize the configuration. This is done as follows. During the simulation we keep track of the distance d between the opposite sides of the box, and perform reinitialization when $d < d_0 = 5\sigma$. A simple way of reinitialization is to take a cubic box from the middle of the periodically extended system and start over. After reinitialization, the periodic boundary condition will be imposed on the new cubic box, instead of the deformed box before reinitialization, and the particles close to the boundary of the new box may have a very short distance to the image particles in the neighboring boxes. Consequently the time step should be decreased in this situation, due to the large forces caused by the interaction at short distance. This is only a problem immediately after the reinitialization. In our calculation, we used an adaptive time step based on the magnitude of the force:

$$\Delta t = \min\left(0.005, \frac{0.01}{\max_i |\mathbf{F}_i|}\right). \tag{17}$$

Sampling or averaging is resumed after a short-time equilibration, usually dozens of time steps after reinitialization.

This constrained molecular dynamics can be formulated as:

$$\begin{cases} m_i \dot{\mathbf{q}}_i(t) = \mathbf{p}_i(t), \\ \dot{\mathbf{p}}_i(t) = -\sum\limits_{j \neq i} \nabla V(|\mathbf{q}_i(t) - \mathbf{q}_j(t)|), \quad i = 1, 2, \ldots, N, \\ \dot{\mathbf{q}}_k(t) = \mathbf{u}(\mathbf{q}_k(t)), \quad k = N+1, N+2, \ldots, M. \end{cases} \tag{18}$$

The additional variables $\mathbf{q}_k's$ are the positions of the vertices of the simulation box, and $\mathbf{u}$ is the given velocity field.

3.2.2. Extracting the stresses

The MD simulation keeps track of the positions and velocities of all particles as functions of time, from which the stress tensor can be calculated using the Irving–Kirkwood expression (7).

In practice, the expression (7) is averaged over the simulation box and reduced to

$$\tau(t) = \frac{1}{|\Omega|} \sum_{\mathbf{q}_i \in \Omega(t)} \frac{1}{m_i} (\mathbf{p}_i \otimes \mathbf{p}_i) + \frac{1}{2|\Omega|} \sum_{j \neq i} d_{ij} (\mathbf{q}_i - \mathbf{q}_j) \otimes \mathbf{F}_{ij}, \tag{19}$$

where in the first term the summation runs over the particles inside the box, and in the second term the summation is over all pairs of particles including their images. Here d_{ij} is defines as

$$d_{ij} = \begin{cases} 1 & \text{if } \mathbf{q}_i, \mathbf{q}_j \in \Omega, \\ 0 & \text{if } \mathbf{q}_i, \mathbf{q}_j \notin \Omega, \\ c & \text{if only one of } \mathbf{q}_i, \mathbf{q}_j \text{ in } \Omega, \end{cases} \tag{20}$$

where $0 \leqslant c \leqslant 1$ is the fraction of $|\mathbf{q}_i - \mathbf{q}_j|$ being cut by the box. Therefore besides the contributions from the particles inside the box, particles outside the box also contribute to the stress, as illustrated in Fig. 4. These contributions become important when the box becomes smaller. Finally the stress is averaged over time:

$$\tau = \frac{1}{T - T_0} \int_{T_0}^{T} \tau(t)\, \mathrm{d}t, \tag{21}$$

where T_0 is some relaxation time.

In Fig. 5, we show several numerical examples of the calculated stress for different velocity fields. The MD simulation is in two dimensions, the size of the simulation box is 20 and the density is $\rho = 0.79$. The temperature is fixed at 1.0 in all cases except in the second one which is not coupled with any thermostats. The stress diverges in this case due to the heat generated by the viscous flow.

In Fig. 6, we plot the shear stress as a function of the shear rate for LJ fluids. The discrete points are obtained from 3D MD calculations at density 0.81 and temperature 1.4. These data fit well to a linear function indicating a linear relation between stress and the rate of strain. The slope of the line, which is 2 in the current case, is the viscosity of the fluid. This value agrees well with result in the literature [12].

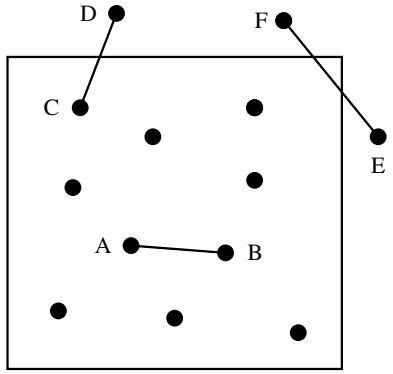

Fig. 4. Computing averaged stress: Besides the contributions from the particles inside the box to the averaged stress, the particles outside the box also contribute, such as *CD* and *EF*.

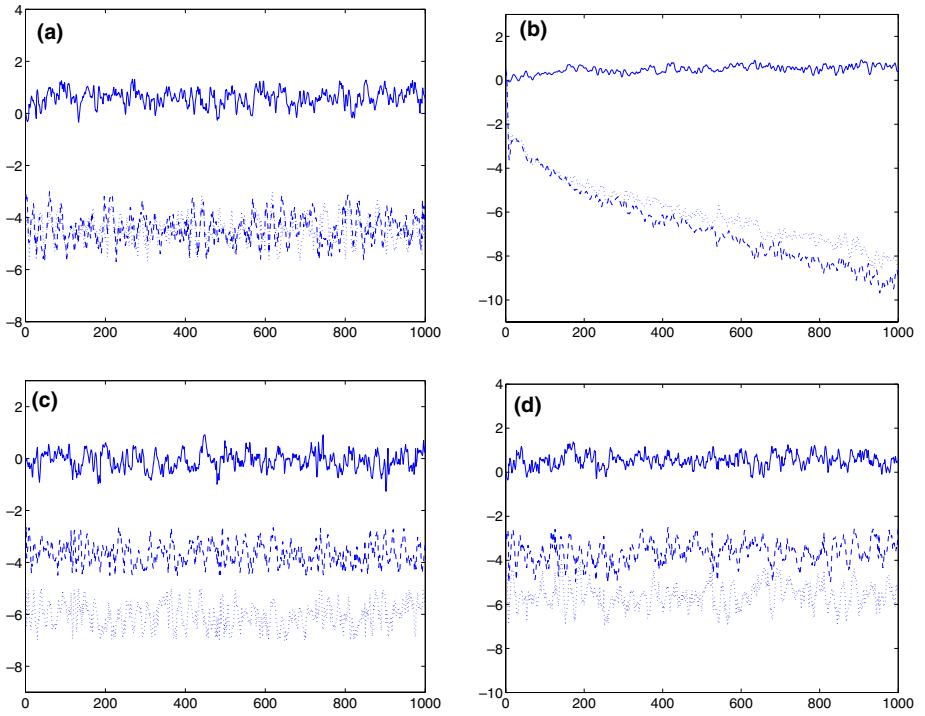

Fig. 5. Time series of stress for various velocity fields. Solid line: $-\tau_{12}$; dashed line: $-\tau_{11}$; dotted line : $-\tau_{22}$. The temperature is fixed in all cases except in (b), where the stress diverges due to the heat generated by the viscous flow. (a) $u = 0.18y$, $v = 0$; (b) $u = 0.18y$, $v = 0$; (c) $u = 0.18x$,$v = -0.18y$; (d) $u = 0.13x + 0.09y$, $v = 0.09x-0.13y$.

3.3. Numerical examples

The calculations proceed as follows:

- Step 0. Given an initial velocity $\mathbf{u}^0$; Let $k = 0$;
- Step 1. Calculate the stress in the interior of the domain by local MD simulations. The MD is constrained by $\mathbf{u}^k$ through the modified periodic boundary conditions on deforming boxes;
- Step 2. Solve the continuum equations in (1) to get $\mathbf{u}^{k+1}$;
- Step 3. Let $k := k + 1$ and go to step 1.

The MD simulation is the most expensive step in the computation, and usually carried out once after a number of macro time steps.

3.3.1. Pressure-driven channel flow

We calculate the dynamics of the pressure-driven channel flow in the xy-plane. The width of the channel is $L = 449$. The system contains Lennard-Jones particles with density 0.79. The flow is driven by an external force in the x-direction with magnitude $F_0 = 2.2 \times 10^{-3}$. The flow is homogeneous in x-direction, so the momentum equation of $\mathbf{u} = (u, v)$ reduces to

$$\rho u_t = (\tau_{12})_y + F_0, \tag{22}$$

with initial condition $u = 0$ and no-slip boundary conditions. τ_{12} is the shear stress.

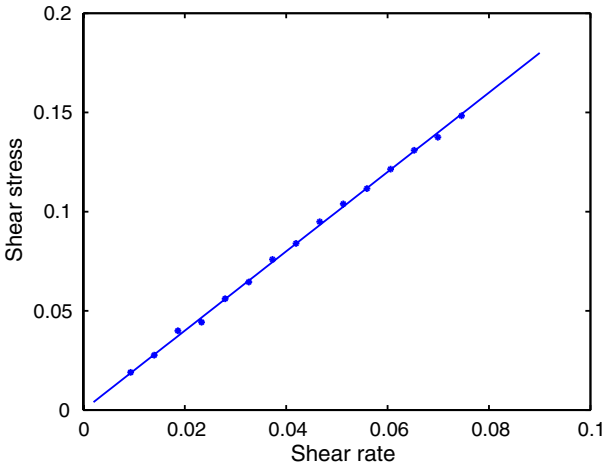

Fig. 6. Shear stress as a function of shear rate for simple LJ fluids. The discrete points are obtained from 3D MD calculation, and they fit very well to a linear function with slope 2 which is the viscosity. All the quantities are expressed in atomic unit.

Eq. (22) is integrated in time by the explicit Euler method with step size $\Delta t = 50$. It is discretized in space on a uniform grid $\{y_i, i = 0, 1, 2, \ldots, N\}$ with $N = 20$ points using central difference. The shear stress $(\tau_{12})_{i+\frac{1}{2}}$ defined at $y_{i+\frac{1}{2}}$ is calculated from 2d MD simulation with the box of size 112.2×22.4 in the xy-plane and contains 2000 particles interacting via Lennard-Jones potential. The shear rate is given by $(u_{i+1} - u_i)/(y_{i+1} - y_i)$, and the temperature is fixed at $T = 0.8$ using the Nosé-Hoover thermostat. The stress is averaged over 2×10^4 time steps after a short period of equilibration. The time step in MD simulation is $\delta t = 0.001$.

The solid curves in Fig. 7 show the velocity profiles at different times. The top curve is the velocity at the steady state. The dashed curves are the velocity profiles obtained by a different calculation: The stress at the first four points $\{y_{i+\frac{1}{2}}, i = 0, 1, 2, 3\}$ is calculated from MD as in the previous calculation, while at the remaining points it is calculated using the constitutive relation $\tau_{12} = \mu u_y$ with $\mu = 4.0$. This value of viscosity is determined by a precomputation using 2d molecular dynamics at the specified temperature and density. It can be seen that the two results are in good agreement, indicating that the shear stress in this case is accurately modeled by the linear relation $\tau_{12} = \mu u_y$.

3.3.2. Dumb-bell fluids

We consider the same problem as in the previous example, but with the LJ particles replaced by dumb-bells. Each dumb-bell consists of two beads, connected by a spring. The density of the beads is 0.79. The interaction potential between the beads has two parts. The first is the LJ potential which acts on all beads in the system. The second is the spring force given by an attractive potential (the FENE potential):

$$V^{\mathrm{FENE}}(r) = \begin{cases} -\frac{1}{2} k r_0^2 \ln\left(1 - \left(\frac{r}{r_0}\right)^2\right), & r < r_0, \\ \infty, & r \geqslant r_0. \end{cases} \tag{23}$$

We used $k = 1$ and $r_0 = 2.5$ in our simulation.

The velocity at the steady state is plotted in Fig. 8(a). Compared to the solution in the previous example, the velocity is smaller, indicating that the same shear rate generates a larger stress in dumb-bell flows.

In each cell, we also calculated the average angle made by the dumb-bells with the flow direction:

$$\theta = \arctan \left| \frac{r_y}{r_x} \right|, \tag{24}$$

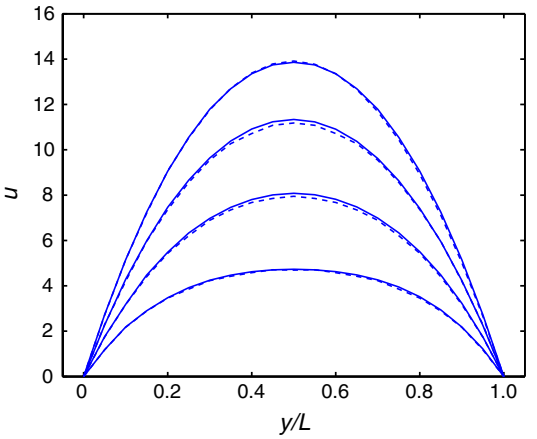

Fig. 7. Velocity profiles in the pressure-driven Poiseuille flow at different times. From bottom to top: $t = 1850,3550,6750,17400$. The solid curves are obtained by the multiscale method where the shear stress is calculated by MD. For the dashed curves, the stresses at the first four grid points are calculated by MD, while at the remaining grid points, they are calculated by the constitutive relation $\tau_{12} = \mu u_y$ with $\mu = 4.0$. The top curves correspond to the steady state solution.

where $(r_x, r_y) = \mathbf{x}_i - \mathbf{x}_j$, and $\mathbf{x}_i$ and $\mathbf{x}_j$ are the positions of the beads belonging to the same dumb-bell. The average angle is plotted as a function of y in Fig. 8(b), from which it can be seen that the local structures of the flow are quite different at different locations: Near the channel boundary where the shear rate is larger, the dumb-bells are more aligned with the flow. In the middle of the channel where the shear rate is relatively small, the dumb-bells are more randomly oriented.

3.3.3. Driven cavity flow

As a two-dimensional example, we solve a canonical problem - the boundary-driven cavity flow. This problem is interesting since the continuum theory predicts an infinite stress at the corners, due to the discontinuity in the velocity boundary condition. However, for the time being we will ignore this issue and still stick with the no-slip boundary condition since at the moment we are primarily concerned with using this example to test our algorithm for the calculation of stress.

The system measures 674×674 in xy-plane, and contains LJ particles with density 0.79. The equations for the conservation of mass and momentum are solved by the projection method on a staggered grid as described in Section 3.1 with 30×30 grid points and time step $\Delta t = 13.5$. The boundary condition $u = 0$, $v = 0$ is imposed everywhere at the boundary except at the upper boundary where we impose $u = 1$, $v = 0$. For initial data we choose the impulsive start: $u = 0$, $v = 0$.

The stress in the interior of the domain is calculated from 2d MD simulation by the method described in Section 3.2. Temperature is fixed at 0.8 using the Nosé-Hoover thermostat. The time step in MD calculation is $\delta t = 0.001$. The stress is averaged over 10^4 time steps after 10^3 steps of equilibration.

The left panel in Fig. 9 displays the velocity field at $t = 4179$ obtained by the multiscale method. For LJ particles, the linear constitutive equation is quite accurate, therefore, we expect Navier–Stokes equations to be valid in this case. Indeed, we will use the Navier–Stokes results to benchmark the results of the hybrid method. We solved the Navier–Stokes equations with the precomputed viscosity $\mu = 4.0$, and the velocity at $t = 4179$ is displayed in the right panel. The two results are in good agreement.

In this example, we studied a 2d example of simple LJ fluids. The result is validated by comparison with the solution of Navier–Stokes equations. However we emphasize that the hybrid method developed here is not limited to the study of simple fluids. It is applicable to complex fluids as well, in which cases the Navier–Stokes equations are not accurate.

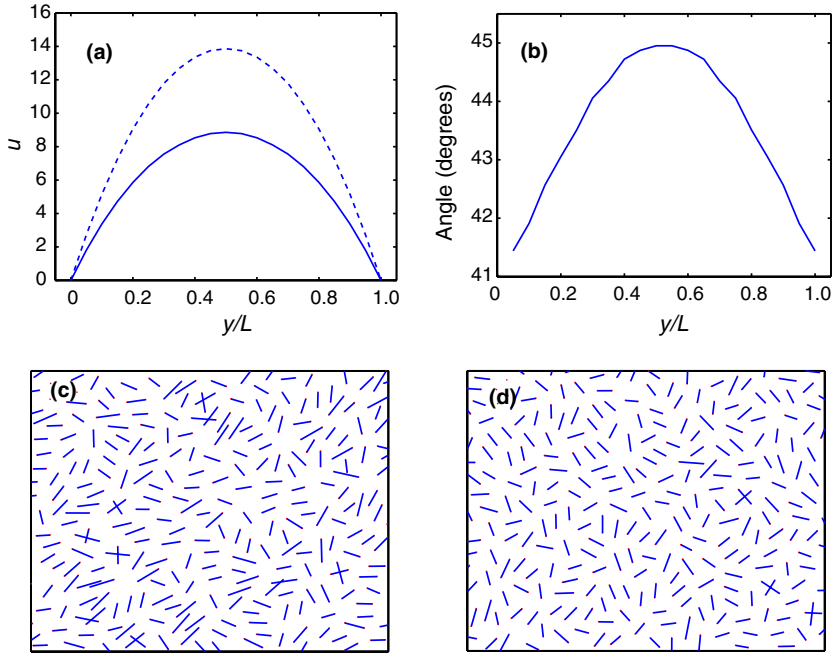

Fig. 8. (a) The steady-state solution of the pressure-driven dumb-bell flow (solid line) compared to the steady-state solution of simple fluids (dashed line) driven by the same pressure. (b) The average angle made by dumb-bells with the flow direction as a function of y. (c) One configuration of the dumb-bell fluids at the boundary; (d) One configuration of the dumb-bell fluids in the middle of the channel.

4. Type-A problems: modeling boundary conditions

In many problems, the empirical boundary conditions supplemented to the continuum equations are not accurate enough to model the complex interactions between the fluid and the solid. In the hybrid method proposed here, we build the boundary conditions from microscopic models such as molecular dynamics,

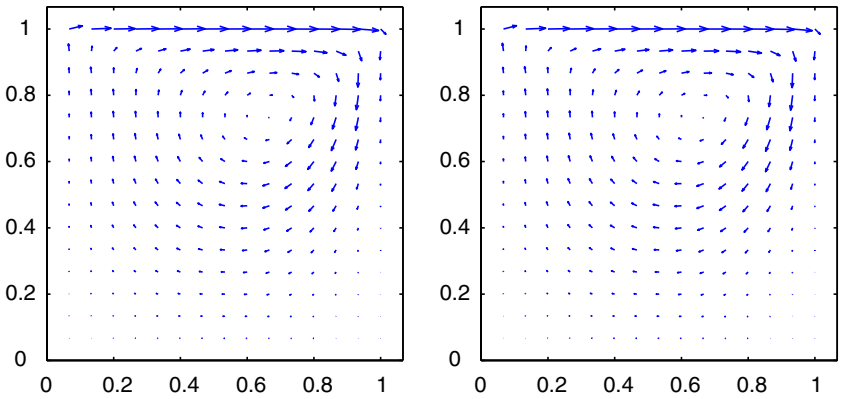

Fig. 9. Left panel: the velocity field of boundary-driven cavity flow at $t = 4179$ obtained by the multiscale method in which the stress is calculated using MD; Right panel: the velocity field at $t = 4179$ obtained by solving the Navier–Stokes equations with stress calculated by the constitutive relation $\tau_d = \mu(\nabla\mathbf{u} + \nabla\mathbf{u}^{\mathrm{T}})$. The spatial coordinates are rescaled by the length of the system.

which is carried out in a local region around the fluid–solid interface. We illustrate this method using three examples. In the first example, we revisit the driven cavity flow, and describe the hybrid method for modeling the boundary conditions. The second is an example of the Marangoni flow in which the flow is driven by heterogeneous interactions on the fluid–solid interface. The third is an example of contact line dynamics.

4.1. Driven cavity flow

For simple fluids, it makes more sense to think of the driven cavity problem as a type-A problem, since the stress singularity in continuum theory only occurs at the corners. There the stress has to be measured from MD, but for the rest of the computational domain, the Navier–Stokes equations and no-slip boundary condition are expected to be accurate enough.

The problem is described in Section 3.3.3. The fluid is confined in a box and sheared by a constant motion of the upper wall. We solve the equations for the conservation of mass and momentum by the projection method on the staggered grid, as described in Section 3.1. In the interior of the domain, the viscous stress is calculated by the linear constitutive relation $\tau_d = \mu(\nabla \mathbf{u} + \nabla \mathbf{u}^T)$. The boundary conditions around the corners are extracted from molecular model, i.e., the shear stress is calculated from MD (see Fig. 10).

In the local MD simulation, the LJ particles are confined in the simulation box by two solid wall at AB and BC, and a repulsive force at CD and DA. For the MD to be consistent with the local continuum field, we impose constraint on the particles in the shaded strips, i.e., their velocities are given by the continuum velocity field plus a random variable with Maxwellian distribution. The shear stress is calculated using the formula (7).

The velocity field is similar to that in Fig. 9, so we will not present the numerical results here.

4.2. Dealing with complex fluid–solid interactions

In this example, the flow is confined between two solid walls parallel to the xz-plane, and is homogeneous in the z-direction. The top wall moves with a constant speed U in the positive x-direction, and the lower wall is fixed in space. The particles interact via the LJ potential. We assume no-slip boundary condition on the upper boundary. The interesting phenomenon arises from the lower boundary, where the interaction between the fluid and the solid varies in the x-direction, i.e., the coefficient η in (8) depends on the position of the solid particles:

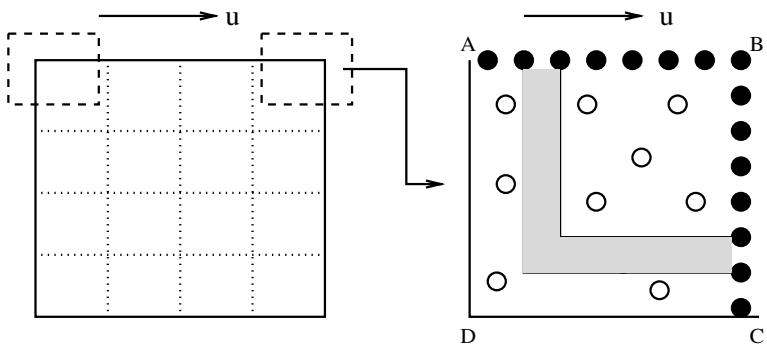

Fig. 10. Schematic of the multiscale method for the driven cavity flow. The shear stresses around the corners are calculated from MD. In the MD simulation, the solid wall AB moves with the given velocity u, the solid wall BC is fixed in space, and a repulsive force is applied at the boundary CD and DA. In the shaded region, the velocities of the particles are generated based on the continuum solution. The shear stress is calculated in the bins on the fluid–solid interface.

$$\eta(x_s) = \frac{1}{2}\left(\cos\left(\frac{2\pi}{L}x_s\right) + 1\right), \tag{25}$$

where L is the length scale for the variation of the fluid–solid interactions.

4.2.1. Macroscopic solver

The continuum equations in (1) are solved by the projection method on staggered grid, as described in Section 3.1. The stress in the interior of the domain is calculated using $\tau_d = \mu(\nabla\mathbf{u} + \nabla\mathbf{u}^{\mathrm{T}})$ with $\mu = 2.0$ corresponding to 3D fluids with particle density $\rho = 0.81$ and temperature $T = 1.4$. The periodic boundary condition is used in the x-direction. No-slip boundary condition is used at the upper boundary EF (see Fig. 11). At the lower boundary AB, the normal velocity vanishes, i.e., $v = 0$. In addition, the shear stress needed at the grid points on AB is calculated from molecular dynamics in the local region $ABCD$.

4.2.2. Estimating the shear stress at the boundary

The schematic of the molecular dynamics simulation is shown in the right panel of Fig. 11. The MD simulation is three dimensional and periodic in the x- and z-direction. In the y-direction, the fluid is confined by a solid wall at AB and a repulsive force at GH. The particles in the system interact via LJ potential, but with different parameters: $\varepsilon_{\mathrm{ff}} = \varepsilon$, $\sigma_{\mathrm{ff}} = \sigma$ for fluid–fluid interactions; $\varepsilon_{\mathrm{ww}} = 5\varepsilon$, $\sigma_{\mathrm{ww}} = 0.775\sigma$ for solid–solid interactions; and $\varepsilon_{\mathrm{fw}} = 1.16\varepsilon$, $\sigma_{\mathrm{fw}} = 1.04\sigma$ for fluid–solid interactions. The repulsive force at GH is modeled by the repulsive part of the LJ potential:

$$P(y) = \varepsilon\left(\frac{\sigma}{r}\right)^{12}, \tag{26}$$

where r is the distance to GH.

For the molecular dynamics to be consistent with the local continuum dynamics, each particle in the strip CD is assigned the following velocity: $\mathbf{u}(x) = \mathbf{u}^{\mathrm{c}}(x) + \tilde{\mathbf{u}}$, where $\mathbf{u}^{\mathrm{c}}(x)$ is the velocity from the continuum calculation and $\tilde{\mathbf{u}}$ is the thermal velocity obeying the Maxwellian distribution at temperature $T = 1.4$. Therefore the strip plays a two-fold role here: As a momentum reservoir it maintains the non-equilibrium dynamics at the steady state; as a thermal reservoir it releases heat generated by viscous flow from the system. At steady state, we expect the average velocity in $ABCD$ to be consistent with the continuum velocity. The region $CDHG$ serves merely as a particle reservoir, and the dynamics in it are irrelevant since it is away from the sampling region. Similar techniques were used in earlier works [3,4].

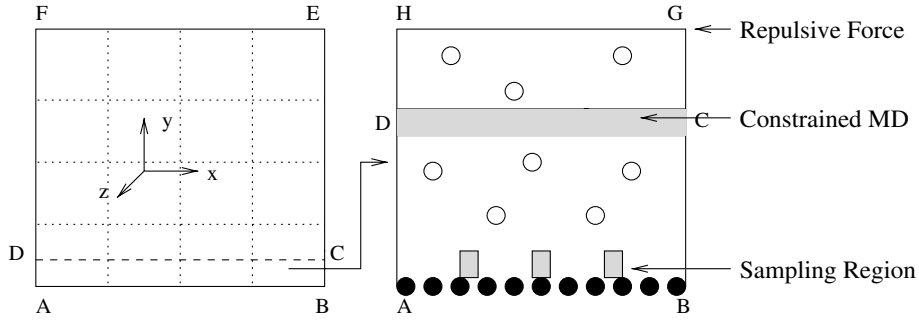

Fig. 11. Schematic of the multiscale method for the example of Marangoni flow. In the left panel, the upper wall EF moves with a constant velocity in the x-direction. The boundary condition at AB is extracted from molecular dynamics simulations confined in $ABCD$. Dotted lines show the grid used in the computation. The set-up of the MD simulation is shown in the right panel. The particles are confined by a repulsive force at GH and the solid wall at AB. The dynamics of the particles in the strip CD are constrained by the continuum velocity field. The boundary conditions are extracted from the small bins at the lower boundary.

The solid wall is modeled by two layers of particles in a fcc lattice. The outer layer is fixed in space, while the inner layer evolves according to Newton's law. Since there is a significant amount of heat generated at the fluid–solid interface, the velocity of the particles in the inner layer is randomly modified with the frequency $10\delta t$ based on the given temperature. $\delta t = 10^{-3}$ is the time step in the molecular dynamics simulation.

The MD simulation starts from an initial configuration in the phase space, e.g., the particles are arranged on a regular lattice with thermal velocities. Typically after 10^4 time steps the system reaches the steady state, and the stress is calculated using the formula (7) in the bins which are 2.5σ above the wall and of size 1σ in both x and y directions.

4.2.3. Numerical results

The overall algorithm is as follows:

- Step 0. Given the initial velocity $\mathbf{u}^0 = 0$, and let $k = 0$;
- Step 1. Calculate the stress at the boundary AB by local MD simulation. The MD is constrained by $\mathbf{u}^k$;
- Step 2. Solve the continuum equations for $\mathbf{u}^{k+1}$;
- Step 3. Let $k := k + 1$ and go to step 1.

To save computational cost, the MD calculation for the boundary condition is carried out once for a few iterations.

The whole system measures 103.2×51.6 in the x- and y-direction. The parameter L in (25) is 103.2. The domain is discretized by a uniform grid with 50×25 points. The upper wall moves with a constant velocity $U = 1.0$ in the positive x-direction. The time step in the macro solver is $\Delta t = 0.052$. Periodic boundary condition is used in the x-direction, and no-slip boundary condition is used at the upper boundary.

In the local MD simulation, the box measures $103.2 \times 15.6 \times 5.2$ in x-, y- and z-direction respectively. It contains 5760 fluid particles and 1280 solid particles. The strip CD is 10σ above the bottom and has a thickness of 1σ. Temperature is fixed at $T = 1.4$ through the constrained dynamics in CD, and also by the modification of the velocities in the inner layer of the solid wall. The stress is sampled for 10^4 time steps, and is fitted by fourth order B-splines before passing back to the macro solver. A typical shear stress is shown in Fig. 12(d).

The numerical results are shown in Fig. 12. Fig. 12(a) shows the velocity field at $t = 11.87$ and Fig. 12(b) shows the corresponding vorticity. No-slip boundary condition breaks down in the middle of the lower boundary, which can be seen from the velocity profile along the boundary (see Fig. 12(c)). The relative slip is caused by the weak attraction between the fluid and solid particles.

4.3. Contact line dynamics

We next consider the motion of two immiscible fluids on a solid surface. Continuum hydrodynamics breaks down in the vicinity of the contact line, where the fluid–fluid interface meets the solid surface. Specifically the usual no-slip boundary condition used in macroscopic fluid dynamics leads to an unphysical divergent shear stress and dissipation rate [19]. Molecular dynamics simulations of Couette or Poiseuille flow show relative slip between the fluid and the wall around the contact line [12,14]. In the Appendix A, we present a full molecular dynamics simulation of a boundary-driven Couette flow. From the results we see a slip region of molecular scale around the contact line. But away from the contact line the no-slip boundary condition is still quite accurate.

To address this issue, various slip models have been introduced. These slip models are sometimes a bit ad hoc. The parameters in these models are problem-dependent and have to be pre-determined based on physical experiments. An alternative approach is to use a hybrid numerical method which combines the

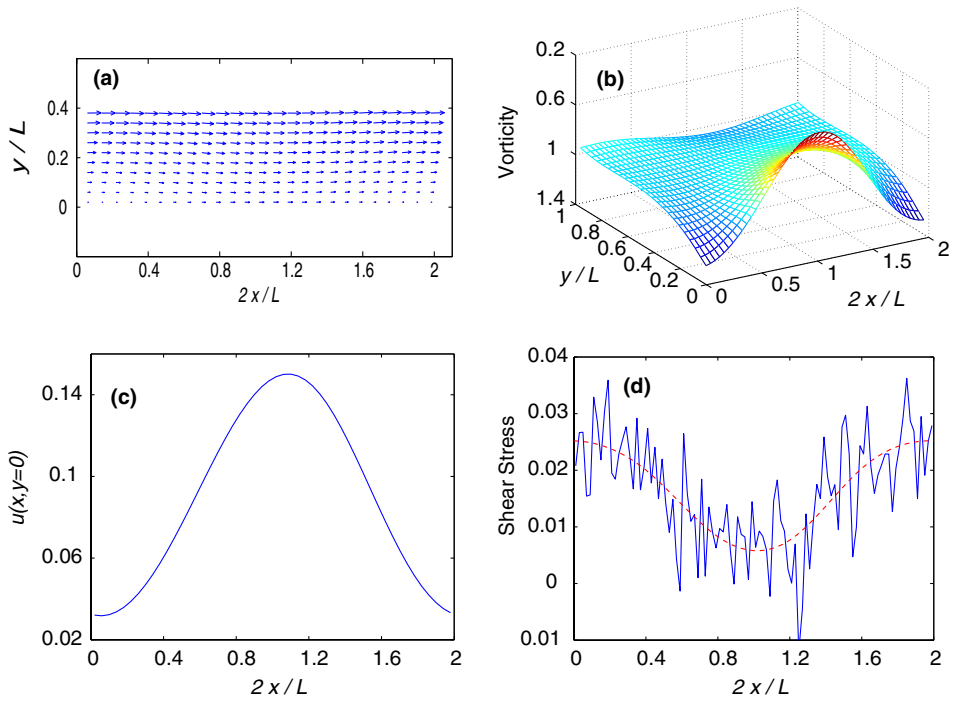

Fig. 12. (a) the velocity field at $t = 11.87$; (b) the vorticity at $t = 11.87$; (c) the velocity at the lower boundary; (d) the stress extracted from MD (solid curve) and fitted by fourth-order B-splines (dashed curve).

continuum calculation with local molecular simulation as was done by Hadjiconstantinou [4]. The computational domain is decomposed into two regions. In the region near the contact line, the system is modeled by molecular dynamics and in the rest of the domain the system is modeled by continuum equations. A Schwartz iteration procedure is employed to match the two solutions in an overlapping region. This method was applied to a steady state contact line problem. Dynamical problems can be dealt with in a fully implicit procedure.

The method proposed here is also a hybrid method. But unlike the domain-decomposition type of methods, we apply the macroscopic solver everywhere in the domain. In the vicinity of the contact line we extract the boundary conditions needed in the macroscopic solver from molecular simulation. This has the advantage that the method can be easily applied to large systems as well as dynamical problems since it naturally decouples the macro and micro spatial/temporal scales.

4.3.1. Macroscopic solver

The dynamics of two immiscible fluids in a channel driven by an external force field is governed by

$$\begin{cases} \rho \mathbf{u}_t + \nabla \cdot \tau = 0, \\ \nabla \cdot \mathbf{u} = 0, \\ \dot{\mathbf{x}}_\Gamma = \mathbf{u}, \end{cases} \tag{27}$$

where the momentum flux in continuum theory is given by

$$\tau = \rho \mathbf{u} \otimes \mathbf{u} + pI - \mu(\nabla \mathbf{u} + \nabla \mathbf{u}^{\mathrm{T}}) + \Gamma(I - \hat{\mathbf{n}} \otimes \hat{\mathbf{n}})\delta_\Gamma - f_0 x I. \tag{28}$$

In the last equation of (27), the fluid–fluid interface $\mathbf{x}_\Gamma(t)$ is advected by the velocity field. In the momentum flux, the first term corresponds to the advection of fluids, the second term is the pressure, the third term is the viscous stress, the forth term corresponds to the surface tension force which is concentrated at the fluid–fluid interface $\mathbf{x}_\Gamma$ (δ_Γ is the surface delta function), and the last term is the external force. I is the identity matrix, Γ is the the surface tension coefficient and $\hat{\mathbf{n}}$ is the unit normal of the interface. The initial and boundary conditions will be specified later.

Smoothing out the surface tension. In the numerical calculation, the surface tension term $\tau_\Gamma = \Gamma(I - \hat{\mathbf{n}} \otimes \hat{\mathbf{n}})\delta_\Gamma$ is replaced by a body force defined by

$$\tilde{\tau}_\Gamma(\mathbf{x}) = \int_{R^2} D(\mathbf{x} - \mathbf{y})\tau_\Gamma(\mathbf{y})\, d\mathbf{y}, \tag{29}$$

where the kernel D is given by

$$D(\mathbf{x}) = \begin{cases} (2d)^{-2}(1 + \cos(\frac{\pi}{d}x))(1 + \cos(\frac{\pi}{d}y)) & \text{if } |x| < d, |y| < d; \\ 0, & \text{otherwise.} \end{cases} \tag{30}$$

This was first introduced by Peskin [16]. Here d, the width of the smoothing region, is taken to be twice the cell size in our calculation. When smoothed out from the interface to the grid points by (29), the total flux is conserved.

Temporal discretization. As for the macroscopic solver, we use the projection method for the first two equations in (27):

$$\rho \frac{\tilde{\mathbf{u}}^{n+1} - \mathbf{u}^n}{\Delta t} + \nabla \cdot \tau^n = 0, \tag{31}$$

$$\rho \frac{\mathbf{u}^{n+1} - \tilde{\mathbf{u}}^{n+1}}{\Delta t} + \nabla p^{n+1} = 0. \tag{32}$$

In the above time-splitting scheme, the pressure is excluded from the momentum flux τ^n in (31). p^{n+1} in (32) is determined by

$$\Delta p^{n+1} = \frac{\rho}{\Delta t} \nabla \cdot \tilde{\mathbf{u}}^{n+1} \tag{33}$$

with Neumann boundary condition. The last equation in (27) is discretized in time by forward Euler method:

$$\frac{(\mathbf{x}_\Gamma)^{n+1} - (\mathbf{x}_\Gamma)^n}{\Delta t} = \mathbf{u}^n. \tag{34}$$

Spatial discretization. The spatial discretization is the same as in Fig. 2. For integer i and j, we define u at $(x_i, y_{j+\frac{1}{2}})$, v at $(x_{i+\frac{1}{2}}, y_j)$, and p at the cell center $(x_{i+\frac{1}{2}}, y_{j+\frac{1}{2}})$. The diagonals of the momentum flux are defined at $(x_{i+\frac{1}{2}}, y_{j+\frac{1}{2}})$, and the off-diagonals are defined at (x_i, y_j). The spatial derivatives are discretized by the central finite difference.

The interface is represented by a collection of discrete points $\{(\mathbf{x}_\Gamma)_i, i = 0, 1, \ldots, N\}$, where the two end points $(\mathbf{x}_\Gamma)_0$ and $(\mathbf{x}_\Gamma)_N$ are the contact points, i.e., the intersections of the interface with the solid walls. Surface tension force is calculated at the middle of each segment. Specifically, a local cubic polynomial is used to fit every four neighboring points, from which the normal to the interface is calculated. Furthermore, to keep the neighboring points from getting too close or too far from each other, the discrete interface points are redistributed from time to time. This is done by polynomial interpolation based on the equal arc-length principle for each element.

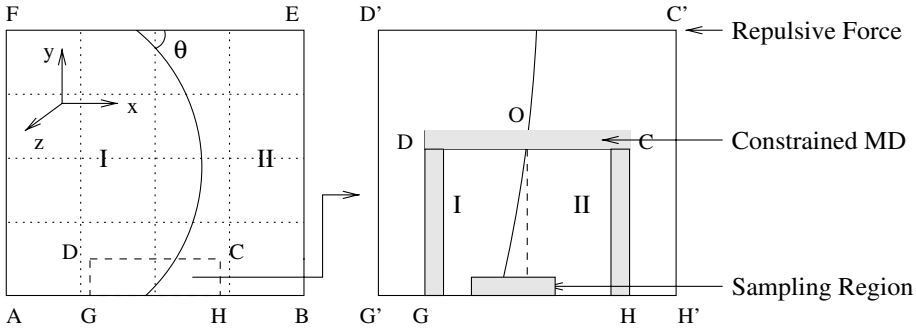

Fig. 13. Schematic of the multiscale method for the contact line problem. Macro grid used in the computation is represented by dotted lines in the left panel. MD is carried out in a local region around the contact line. Periodic boundary conditions are imposed on the boundaries of the enlarged box $G'D'$ and $H'C'$. The dynamics in the shaded strips GD, DC and CH are constrained by continuum velocity field. The shear stress and the position of the contact point are computed in the strip along GH.

Boundary condition and missing data. In the stream-wise direction and away from the interface, the velocity field relaxes to uniform Poiseuille flow if the external force f_0 is homogeneous in space. Therefore we impose Neumann boundary condition on the velocity on AF and BE (see Fig. 13).

To keep the interface away from the boundaries of the computational domain, we re-center the interface to the middle of the domain from time to time during the calculation. At the solid walls AB and EF and away from the contact points, no-slip boundary conditions are valid. In the vicinity of the contact points, the tangential stress, which is the boundary condition needed when solving the momentum equation, will be extracted from molecular dynamics as described below. Furthermore, the dynamics of the contact points $(\mathbf{x}_\Gamma)_0$ and $(\mathbf{x}_\Gamma)_N$ are obtained from MD.

Remark. In the numerical examples presented here, the surface force is calculated by the continuum model using the position of the interface. However, in the case of rough solid walls and hence large fluctuations of the interface, it is more accurate to calculate the surface force at the boundaries from the MD simulation.

4.3.2. Microscopic solver and estimating boundary conditions

The schematics of the molecular simulation around the contact line is shown in Fig. 13. Our goal is to use molecular dynamics simulation in the local region $GHCD$ to extract the following data needed in the macro solver:

- shear stress along GH;
- position of the contact line;

Constrained MD simulation. Periodic boundary conditions are imposed in z-direction. In x-direction, the flow field is not necessarily periodic, so we enlarge the simulation box to $G'H'C'D'$ and impose periodic boundary conditions on $G'D'$ and $H'C'$ instead (see the right panel in Fig. 13). The enlarged part serves as a particle reservoir. In the system we have two fluid species, fluid I in the left and fluid II in the right. When a fluid particle crosses the boundary $H'C'$ or $G'D'$, its type needs to be changed. For example, when a fluid particle of species II crosses $H'C'$, it will enter the box through $G'D'$ and become species I.

In y-direction, the particles are confined by the solid wall at $G'H'$ and a repulsive force at $C'D'$. The repulsive force is modeled by the repulsive part of the LJ potential, as given in (26). The repulsive force

is used to keep the particles from escaping from the MD domain. The detailed molecular models are given in Appendix A.

For the consistency between the molecular dynamics and the continuum dynamics, a modified Anderson thermostat is used in the strips *GD*, *DC*, and *CH*: At Poisson distributed times with certain frequency v, a random particle is selected from the strips and its velocity is replaced by $\mathbf{u}(\mathbf{x}) = \mathbf{u}^c(\mathbf{x}) + \tilde{\mathbf{u}}$, where $\mathbf{u}^c$ is the velocity from continuum dynamics and $\tilde{\mathbf{u}}$ is a random variable with Maxwell–Boltzmann distribution at the fixed temperature $T = 1.4$.

For steady-state or slowly varying dynamic problems, the total flux of species I across *GDO* and the total flux of species II across *OCH* are both zero in the continuum theory in the frame of the moving interface. Here *O* denotes the intersection of the interface with *DC*. Therefore, by imposing the continuum velocity field on the boundaries of the box *GDCH*, we in fact fixed the number of particles of each species inside the box. However, in the early stage of the MD simulation, net fluxes of particles of both species across *GDO* and *OCH* are necessary for the interface to relax to its correct shape. For example, we may start the MD simulation from a configuration in which we have a vertical interface in the middle of the simulation box (dashed line in the right panel of Fig. 13), and we have the same number of particles for both species inside *GDCH*. The curved solid line indicates the correct shape at the steady state. In this case, during the transient period of the molecular dynamics we have to allow a net flux of particles out of the box through *GDO* for species I and a net flux into the box through *OCH* for species II. Therefore, to obtain the correct steady state the constraints imposed on the strips need to be relaxed. In our simulation, we impose the constraints in the horizontal strip (*DC*) and the vertical strips (*GD* and *CH*) alternatively, i.e., only one of the constraints (e.g., constraint on *DC*) is imposed for a number of steps, then it is switched off and another constraint (e.g., constraints on *GD* and *CH*) is imposed for the same number of steps, and so on.

The particles in the outer layer of the wall are fixed at the lattice sites. The particles in the inner layer obey Newton's law and their velocities are randomly modified with certain frequency based on the given temperature. The system is re-centered from time to time so that the interface stays in the middle of the box.

Estimating the boundary conditions. The Newton's equations are integrated using the velocity-Verlet algorithm. The shear stress is calculated using the formula (7) in the bins which are 2.5σ above the wall and of size 1σ in both x- and y-direction.

To estimate the position of the contact line, we first calculate the particle density function along the fluid–solid interface (remember *O* is fixed):

$$\rho(x) = \sum_i \rho_i \delta((\mathbf{q}_i)_x - x), \tag{35}$$

where the sum is over all particles in the strip above the solid wall, $(\mathbf{q}_i)_x$ is the x coordinate of the ith particle, ρ_i is 1 for particles of species I and -1 for particles of species II. The position of the contact line is determined by $\rho(x) = 0$. In practice, we take a strip which is 2.5σ above the wall and partition it into uniform bins in x direction. Then the density is obtained by taking the sum of ρ_i in each bin. The position of the contact line is given by

$$(x_\Gamma)_0 = x_0 + \int_{x_0}^{x_1} \tilde{\rho}(x)\, \mathrm{d}x, \tag{36}$$

where x_0 and x_1 are the positions of the leftmost and the rightmost bins respectively. $\tilde{\rho}(x)$, which is between 0 and 1, is the rescaled density:

$$\tilde{\rho}(x) = \frac{\rho(x) - \min_x \rho(x)}{\max_x \left\{\rho(x) - \min_x \rho(x)\right\}}. \tag{37}$$

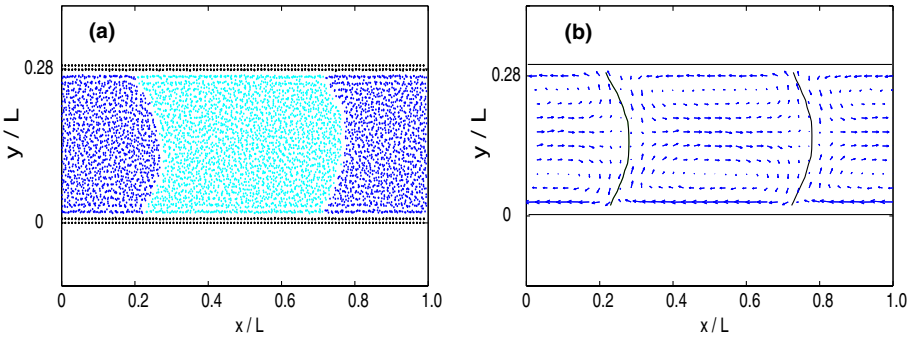

Fig. 14. Full MD simulation of the pressure-driven channel flow. (a) A snapshot of the instantaneous positions of all particles; (b) The averaged velocity field and the fluid–fluid interfaces.

4.3.3. Numerical results

The calculation follows the following procedure:

- Step 0. Given the initial velocity field $\mathbf{u}^0 = 0$, and the initial interface $(\mathbf{x}_\Gamma)^0$ at static state; Set $k = 0$;
- Step 1. Constrained by $\mathbf{u}^k$, the MD simulation is carried out in a local region around the contact line, from which the shear stress and the position of the contact line are calculated;
- Step 2. Solve equations in (27) for $\mathbf{u}^{k+1}$ and $(\mathbf{x}_\Gamma)^{k+1}$;
- Step 3. Let $k := k + 1$ and goto step 1.

We applied the hybrid method to three problems with different parameters: In the first example, we use a small-size system to benchmark the hybrid method; the second one is a large-scale dynamical problem; the last is an example of asymmetric fluid–solid interactions.

Example 1. Two immiscible fluids are confined in a channel and driven by an external force $f_0 = 0.02$ in x direction. The system measures $69.7 \times 22.5 \times 5.16$ and contains 2944 particles of each fluid and 1728 solid particles. The system is periodic in x and z directions. We use this small system to check the validity of the constrained MD simulation and the hybrid method.

A full MD simulation is carried out and a snap shot of the instantaneous positions of the particles is shown in Fig. 14. Also shown in Fig. 14 is the averaged velocity field and the position of the fluid–fluid interface in steady state. The velocity is measured in the frame of moving interface.

To check the validity of the constrained molecular dynamics used in the hybrid method, we performed a local MD simulation around the contact line. The box $GDCH$ (see Fig. 13) is 34.8×11.2 in size and the extended box $G'D'C'H'$ is 45.7×22.5. The dynamics of the particles in the strips GD, DC and CH are constrained by the average velocity field obtained from the full MD simulation. The simulation starts from a configuration with a vertical fluid–fluid interface in the middle of the box. In the left panel of Fig. 15, we plot the time series of the difference of the particle numbers of both species inside $GDCH$. We clearly see a transient time during which the particles of species I flow out of the box and particles of species II flow into the box. In the right panel of Fig. 15, we compare the shear stress calculated on the surface of the solid wall in the full MD simulation and in the local constrained MD simulation, and we see good agreements.

We also applied the hybrid method to calculate the steady-state solution. The parameters in the continuum model are $\rho = 0.81$, $\mu = 2.0$ and $\Gamma = 3.7$. 70×20 grid points are used in the spatial discretization, and the time step is $\Delta t = 0.05$. We start from a static configuration and slowly increased the external force to 0.02. The steady-state velocity field and the interface (dashed line) are shown in Fig. 16. These results agree well with the full MD results in Fig. 14.

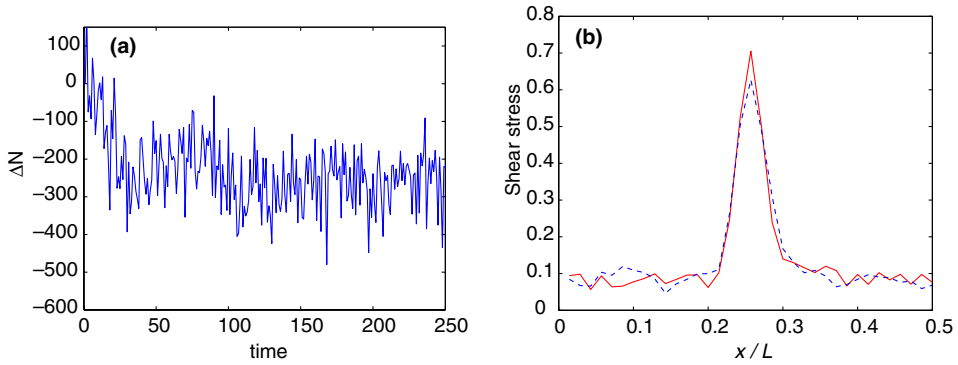

Fig. 15. Results of the constrained MD simulation. (a) The time series of $\Delta N = N_{\mathrm{I}}(t) - N_{\mathrm{II}}(t)$, where $N_{\mathrm{I}}(t)$ and $N_{\mathrm{II}}(t)$ are the particle numbers of the two species in the box $GDCH$ (see Fig. 13) respectively; (b) The shear stress measured at the solid wall. The solid curve is calculated from the full MD simulation and the dashed curve is from the constrained MD simulation.

Example 2. The equations in (27) are solved in the domain 1500×500 and with parameters $\rho = 0.81$, $\mu = 2.0$ and $\Gamma = 3.7$. The computational domain is covered by 300×100 grid points and the interface is discretized by 100 points. The system is driven by an external force $f_0(t) = 5.35 \times 10^{-11} t$ in x-direction. The system is at static state initially and the contact angle is 90° due to the identical interaction between the two fluids and the solid. The time step is $\Delta t = 2$. The boundary conditions are updated every 10^4 macro time steps by molecular dynamics simulation.

In the molecular dynamics simulation, the enlarged box $G'H'C'D'$ measures $38.7 \times 26.3 \times 6.5$ and contains 600 solid particles and 2160 particles of each fluid. The strip CD is 12.5 above the wall and has length 30.7 and thickness 1.0. Temperature is set at $T = 1.4$. Twenty independent MD simulations were done on a cluster with 20 processors. On each processor, samples are taken for a period of $5 \times 10^4 \delta t$ after an equilibration period of $3 \times 10^4 \delta t$ where $\delta t = 0.005$ is the MD time step. The sampled data were averaged over time and over the 20 different trajectories.

Fig. 17(a) shows the instantaneous velocity field and the position of the interface at $t = 3.4 \times 10^5$. The velocity at the boundary AB is shown in Fig. 17(b), from which the slip in the region around the contact point can be seen.

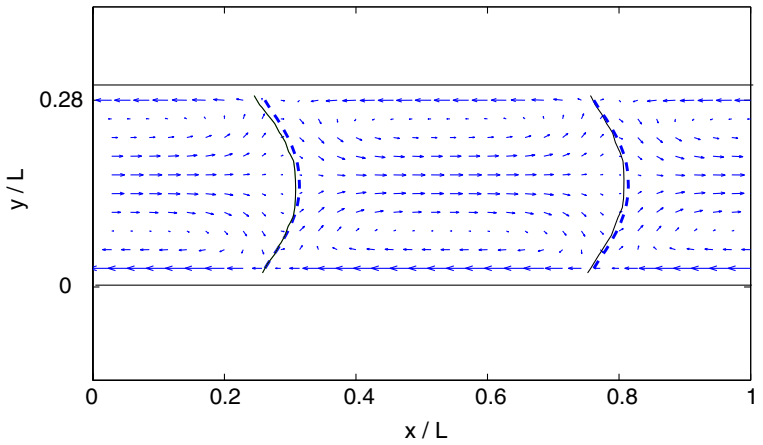

Fig. 16. The steady-state solution of Example 1 by the hybrid method and comparison with the results of full MD. The interface is shown in dashed curve. The solid curve shows the interface obtained by full MD simulation.

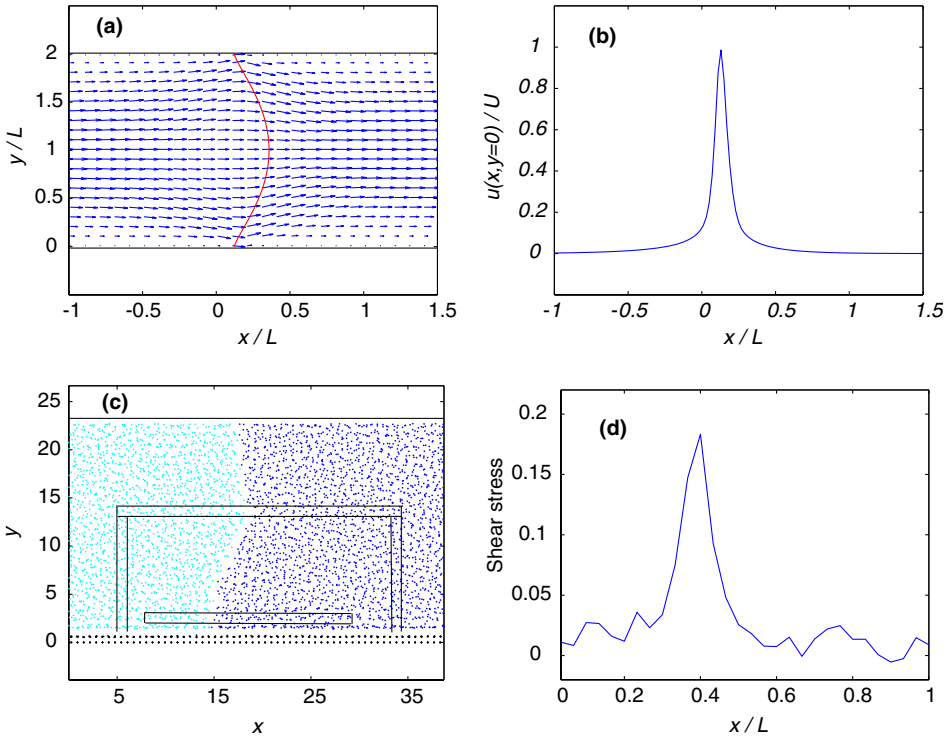

Fig. 17. (a) The instantaneous velocity field and fluid–fluid interface at $t = 3.4 \times 10^5$; (b) the velocity along the boundary $y = 0$; (c) A snapshot of the instantaneous positions of all particles in the local MD simulation; (d) the shear stress along the fluid–solid interface calculated from MD. The coordinates are rescaled by $L = 250$ and $U = 0.05$.

A snapshot, projected onto the xy-plane, of the instantaneous positions of all particles in the local MD simulation is shown in Fig. 17(c). The dynamics of the particles in the strips are constrained by the continuum velocity field, and samples are taken in the strip close the lower boundary. The calculated shear stress is shown in Fig. 17(d). The shear stress is large but finite at the contact point.

The fluid–fluid interfaces at different times are shown in Fig. 18(a). The dynamic contact angle as a function of the applied force is shown in Fig. 18(b). The angle is calculated from the local MD simulation by fitting the fluid–fluid interface which is close to the solid wall by a straight line. The contact angle decreases and the curvature of the interface increases as the external force increases.

Example 3. As a third test, we changed the interaction between the fluids and the solid. The attraction between fluid I and the solid is decreased by taking $\eta = 0.7$ in the potential (8), and all the other parameters are kept unchanged. The static contact angle θ in this case is 65°.

We start from the static state and impose the same external force as in Example 2 in the positive x-direction until it reaches $f_0 = 2.2 \times 10^{-5}$. Then the force is decreased at the same rate until it reaches $f_0 = -7.0 \times 10^{-5}$. The fluid–fluid interfaces at different times are shown in Fig. 19(a). The left-most dashed line is the interface at the static position, and it travels in the stream-wise direction as the external force increases. The right-most dashed line corresponds to $f_0 = 2.2 \times 10^{-5}$. The solid lines from the right to the left show the shapes of the interfaces as the external force decreases. In Fig. 19(b), we show the dynamic contact angle as a function of the applied force. Again, the dashed curve corresponds

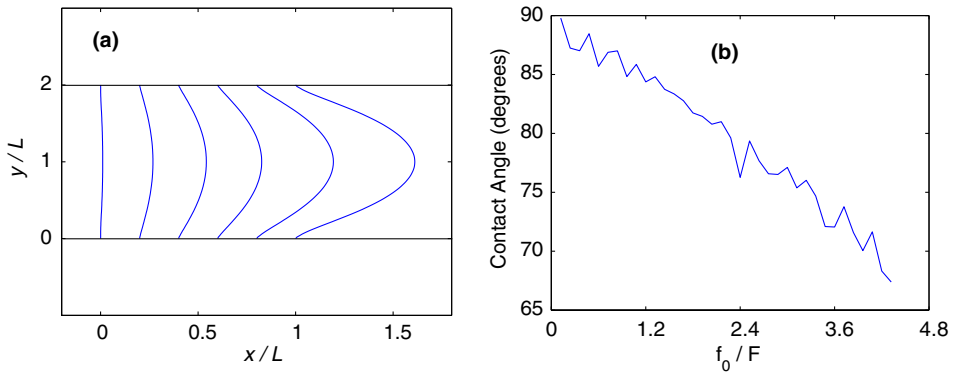

Fig. 18. Dynamics of the CL problem with equal fluid–solid interactions. (a) Fluid–fluid interfaces at different times. From left to right, the external force increases from 0 to 3.6×10^{-5}; (b) Dynamic contact angle as a function of applied force. The applied force is rescaled by $F = 8.1 \times 10^{-6}$.

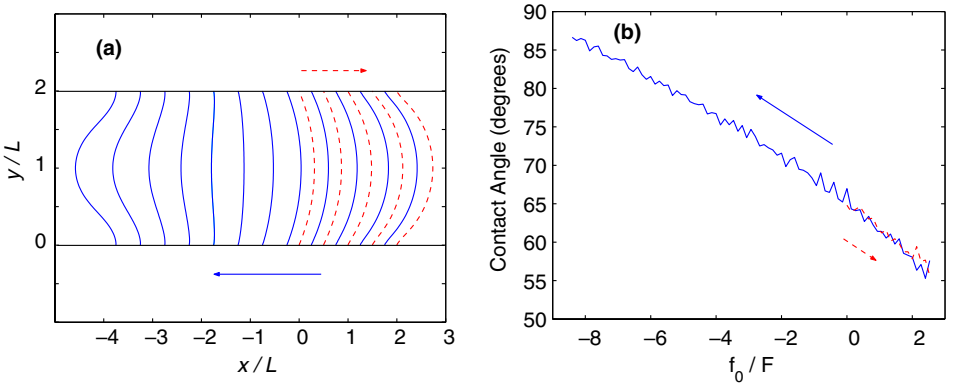

Fig. 19. Dynamics of the contact line problem with asymmetric fluid–solid interactions. (a) Fluid–fluid interfaces at different times. For dashed curves from left to right, the external force increases from 0 to 2.2×10^{-5}; For solid curves from right to left, the external force decreases from 2.2×10^{-5} to -7.0×10^{-5}; (b) Dynamic contact angle as a function of external force. The external force is rescaled by $F = 8.1 \times 10^{-6}$.

to the dynamics as the force increases, and the solid curve corresponds to the dynamics as the force decreases.

In the numerical examples presented above, there are two widely separated time scales: The short relaxation time of molecular dynamics and the long time scale of the dynamics caused by the slow variation of external force. The hybrid method exploited the scale separation and effectively calculated long-time dynamics using data from short-time MD simulations. Indeed, the step size (2×10^4) between successive MD simulations is two orders of magnitude larger than the time (4×10^2) needed for extracting data from local MD simulations. Moreover, the MD simulation is carried out in a much smaller domain than the whole system. A full MD simulation of the whole system for the long time dynamics is prohibitively expensive.

An alternative approach for solving the contact line dynamics is to develop slip models using detailed MD results. A thorough discussion in this direction can be found in [14].

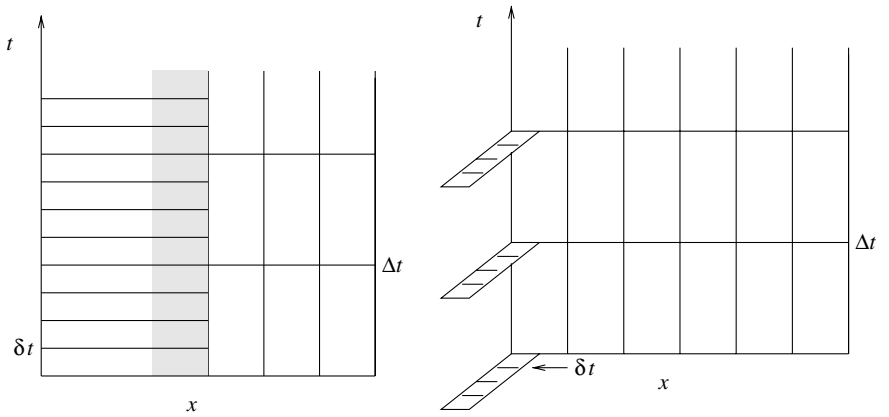

Fig. 20. Left panel: The overlapping domain decomposition method in spatial and temporal domain. The continuum dynamics and molecular dynamics are calculated in different domains simultaneously. The shaded region indicates the overlapping region where the two descriptions are forced to match. The boundary conditions needed in continuum model are averaged over space and time. Right panel: The hybrid method for type-A problem developed here. A macro solver covers the whole domain, and the needed data (boundary conditions) are calculated from MD in the fibers.

5. Conclusion

In conclusion, we have developed general multiscale methods for two types of problems in fluid dynamics: problems with unknown constitutive relations and problems with unknown boundary conditions. For both problems, a macroscopic solver is first chosen and applied everywhere in the computational domain. The missing data, the flux in the first type of problems and the boundary conditions in the second type of problems, are extracted from local molecular dynamics simulations. The molecular dynamics is constrained through appropriate boundary conditions. The multiscale methods were tested with several non-trivial problems, including a pressure-driven dumb-bell flow in a channel and contact line dynamics.

The macro and micro time steps are decoupled in our method. At fixed macro time steps, the needed data is calculated by the constrained MD simulation in the MD domain, which does not have to be viewed as a subset of the flow domain. A more appropriate schematic for our method is shown in Fig. 20, in which the MD is done in the fibers (to use the terminology from fiber bundles).

In general the main cost of hybrid method is still in the molecular simulations. The multiscale method developed here has the ability to minimize the size of such molecular simulations, and hence optimize efficiency.

Acknowledgment

The authors would like to thank B. Engquist, X. Li, T. Qian and X. P. Wang for helpful discussions. The work of E is supported by ONR grant N00014-01-1-0674 and National Science Foundation of China through a Class B Award for Distinguished Young Scholars 10128102.

Appendix A. A full molecular dynamics simulation of contact-line motion

In the simulation, two immiscible fluids were confined between two planar walls parallel to the xz-plane. The system measures 15.1σ between the walls, and $51.6\sigma \times 6.45\sigma$ in x- and z-direction respectively. Each

wall consisted of 800 particles forming two [010] planes of an fcc lattice with density $\rho_w = 1.86\sigma^{-3}$. Each fluid consisted of 1728 particles with density $\rho_f = 0.81\sigma^{-3}$. Interaction between particles were modeled by the modified Lennard-Jones potential (8), with the parameters given by:

$$\begin{pmatrix} \varepsilon_{11} & \varepsilon_{12} & \varepsilon_{1s} \\ \varepsilon_{21} & \varepsilon_{22} & \varepsilon_{2s} \\ \varepsilon_{s1} & \varepsilon_{s2} & \varepsilon_{ss} \end{pmatrix} = \begin{pmatrix} 1 & 1 & 1.16 \\ 1 & 1 & 1.16 \\ 1.16 & 1.16 & 5 \end{pmatrix} \varepsilon, \tag{38}$$

$$\begin{pmatrix} \sigma_{11} & \sigma_{12} & \sigma_{1s} \\ \sigma_{21} & \sigma_{22} & \sigma_{2s} \\ \sigma_{s1} & \sigma_{s2} & \sigma_{ss} \end{pmatrix} = \begin{pmatrix} 1 & 1 & 1.04 \\ 1 & 1 & 1.04 \\ 1.04 & 1.04 & 0.77 \end{pmatrix} \sigma, \tag{39}$$

and

$$\begin{pmatrix} \eta_{11} & \eta_{12} & \eta_{1s} \\ \eta_{21} & \eta_{22} & \eta_{2s} \\ \eta_{s1} & \eta_{s2} & \eta_{ss} \end{pmatrix} = \begin{pmatrix} 1 & -1 & 1 \\ -1 & 1 & 1 \\ 1 & 1 & 1 \end{pmatrix}. \tag{40}$$

Between different fluid species, $\eta = -1$ was used to make the two fluids immiscible. At the fixed temperature $T = 1.4\varepsilon/k_B$, the viscosity of the fluid is $\mu = 2.0(\varepsilon m)^{1/2}\sigma^{-2}$ and the surface tension coefficient of the fluid–fluid interface is $\Gamma = 3.7\varepsilon\sigma^{-2}$ [12].

The system is periodic in z-direction. In x-direction, the system is also periodic but the species of the fluid particle needs to be changed when it crosses the boundary of the box. For example, if a particle of species II crosses the boundary on the right, it will enter the box on the other side with velocity unchanged, but its species will change to I.

The particles in the outer layer of each wall were fixed at the lattice sites during the simulation, and the lattice sites move at a constant speed U in opposite directions along the x-direction. The inner layer of each wall servers as a thermostat and the velocities are randomly modified with frequency $10\delta t$ based on given temperature $T = 1.4\varepsilon/k_B$. $\delta t = 0.005$ is the time step.

Fig. 21(a) is a snapshot of the instantaneous positions of all particles at steady state. The shear velocity is $U = 0.07$ in reduced atomic units. Fig. 21(b) shows the corresponding velocity field obtained by time-averaging the instantaneous atomic velocities within bins of size $1.03\sigma \times 0.92\sigma$ in the xy-plane. Away from the fluid–fluid interface, it is Couette flow and the no-slip boundary condition is satisfied at the solid walls. However, near the contact line there is a slip region in which the no-slip boundary condition is invalid.

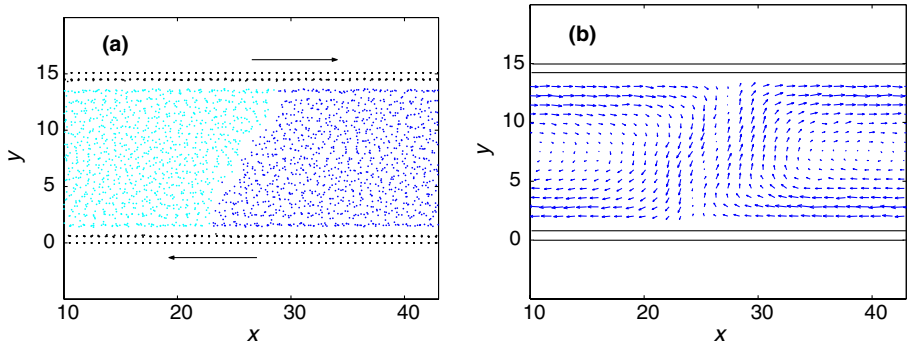

Fig. 21. (a) Projections of particles positions onto xy-plane. (b) Averaged velocity field over 8×10^5 time steps.

References

[1] W. E and B. Engquist, The heterogeneous multi-scale methods, Comm. Math. Sci. 1(1) (2003) 87–133.
[2] S.T. O'Connell, P.A. Thompson, Molecular dynamics-continuum hybrid computations: a tool for studying complex fluid flows, Phys. Rev. E 52 (1995) 5792–5795.
[3] N. Hadjiconstantinou, A.T. Patera, Heterogeneous atomistic-continuum representation for dense fluid systems, Int. J. Modern Phys. C 8 (1997) 967.
[4] N. Hadjiconstantinou, Hybrid atomistic-continuum formulations and the moving contact-line problems, J. Comp. Phys. 154 (1999) 245–265.
[5] E.G. Flekkoy, G. Wagner, J. Feder, Hybrid model for combined particle and continuum dynamics, Europhys. Lett. 52 (3) (2000) 271–276.
[6] X. Nie, S. Chen, W. E, M.O. Robbins, A continuum and molecular dynamics hybrid method for micro- and nano-fluid flow, J. Fluid Mech. 500 (2004) 55–64.
[7] J. Li, D. Liao, S. Yip, Nearly exact solution for coupled continuum/MD fluid simulation, Journal of Computer-Aided Material Design 6 (1999) 95–102.
[8] M.P. Allen, D.J. Tildesley, Computer Simulation of Liquids, Oxford, 1987.
[9] D. Frenkel, B. Smit, Understanding Molecular Simulation, Academic Press, 2002.
[10] A.W. Lees, S.F. Edwards, The computer study of transport processes under extreme conditions, J. Phys. C 5 (1972) 1921–1929.
[11] J.H. Irving, J.G. Kirkwood, The statistical mechanical theory of transport processes IV, J. Chem. Phys. 18 (1950) 817–829.
[12] P.A. Thompson, M.O. Robbins, Simulations of contact-line motion: slip and the dynamic contact angle, Phys. Rev. Lett. 63 (1989) 766–769.
[14] T.Z. Qian, X.P. Wang, P. Sheng, Molecular scale contact line hydrodynamics of immiscible flows, Phys. Rev. E 68 (2003) 016306.
[16] C.S. Peskin, Flow patterns around heart valves: a numerical method, J. Comp. Phys. 25 (1977) 220.
[19] E.B. Dussan V., On the spreading of liquids on solid surfaces: static and dynamic contact lines, Ann. Rev. Fluid Mech. 11 (1979) 371–400.
[20] A.J. Chorin, Numerical solution of the Navier–Stokes equations, Math. Comp. 22 (1968) 745–762.
[21] K.A. Dill, S. Bromberg, Molecular Driving Forces, Garland Science, New York and London, 2003.

Further reading

[13] P.A. Thompson, S.M. Troian, A general boundary condition for liquid flow at solid surfaces, Nature 389 (1997) 360–362.
[15] T.Z. Qian, X.P. Wang, P. Sheng, Power-law slip profile of the moving contact line in two-phase immiscible flows, Phys. Rev. Lett. 93 (2004) 094501.
[17] S.O. Unverdi, G. Tryggvason, A front-tracking method for viscous, incompressible, multi-fluid flows, J. Comp. Phys. 100 (1992) 25–37.
[18] J. Koplik, J.R. Banavar, Continuum deductions from molecular hydrodynamics, Annu. Rev. Fluid Mech. 27 (1995) 257–292.
[22] C. Denniston, M.O. Robbins, Molecular and continuum boundary conditions for a miscible binary fluid, Phys. Rev. Lett. 87 (2001) 178302.
[23] Q. Sun, I.D. Boyd, G.V. Candler, A hybrid continuum/particle approach for modeling subsonic, rarefied flows, J. Comp. Phys. 194 (2004) 256–277.
[24] A.L. Garcia, J.B. Bell, W.Y. Crutchfield, B.J. Alder, Adaptive mesh and algorithm refinement using direct simulation Monte Carlo, J. Comp. Phys. 154 (1999) 134–155.